J/ψ production at low pT in Au + Au and Cu + Cu collisions at √SNN = 200 GeV with the STAR detector

(STAR Collaboration) Adamczyk, L.; ...; Planinić, Mirko; ...; Poljak, Nikola; ...; Zyzak, M.

Permanent link / Trajna poveznica: https://urn.nsk.hr/urn:nbn:hr:217:925060

Download date / Datum preuzimanja: **2025-04-01**

J/ψ production at low p_T in Au + Au and Cu + Cu collisions at $\sqrt{s_{NN}} = 200$ GeV with the STAR detector

L. Adamczyk,[1] J. K. Adkins,[23] G. Agakishiev,[21] M. M. Aggarwal,[35] Z. Ahammed,[53] I. Alekseev,[19] J. Alford,[22] C. D. Anson,[32] A. Aparin,[21] D. Arkhipkin,[4] E. C. Aschenauer,[4] G. S. Averichev,[21] A. Banerjee,[53] D. R. Beavis,[4] R. Bellwied,[49] A. Bhasin,[20] A. K. Bhati,[35] P. Bhattarai,[48] H. Bichsel,[55] J. Bielcik,[13] J. Bielcikova,[14] L. C. Bland,[4] I. G. Bordyuzhin,[19] W. Borowski,[45] J. Bouchet,[22] A. V. Brandin,[30] S. G. Brovko,[6] S. Bültmann,[33] I. Bunzarov,[21] T. P. Burton,[4] J. Butterworth,[41] H. Caines,[57] M. Calderón de la Barca Sánchez,[6] J. M. Campbell,[32] D. Cebra,[6] R. Cendejas,[36] M. C. Cervantes,[47] P. Chaloupka,[13] Z. Chang,[47] S. Chattopadhyay,[53] H. F. Chen,[42] J. H. Chen,[44] L. Chen,[9] J. Cheng,[50] M. Cherney,[12] A. Chikanian,[57] W. Christie,[4] J. Chwastowski,[11] M. J. M. Codrington,[48] G. Contin,[26] J. G. Cramer,[55] H. J. Crawford,[5] X. Cui,[42] S. Das,[16] A. Davila Leyva,[48] L. C. De Silva,[12] R. R. Debbe,[4] T. G. Dedovich,[21] J. Deng,[43] A. A. Derevschikov,[37] R. Derradi de Souza,[8] B. di Ruzza,[4] L. Didenko,[4] C. Dilks,[36] F. Ding,[6] P. Djawotho,[47] X. Dong,[26] J. L. Drachenberg,[52] J. E. Draper,[6] C. M. Du,[25] L. E. Dunkelberger,[7] J. C. Dunlop,[4] L. G. Efimov,[21] J. Engelage,[5] K. S. Engle,[51] G. Eppley,[41] L. Eun,[26] O. Evdokimov,[10] O. Eyser,[4] R. Fatemi,[23] S. Fazio,[4] J. Fedorisin,[21] P. Filip,[21] Y. Fisyak,[4] C. E. Flores,[6] C. A. Gagliardi,[47] D. R. Gangadharan,[32] D. Garand,[38] F. Geurts,[41] A. Gibson,[52] M. Girard,[54] S. Gliske,[2] L. Greiner,[26] D. Grosnick,[52] D. S. Gunarathne,[46] Y. Guo,[42] A. Gupta,[20] S. Gupta,[20] W. Guryn,[4] B. Haag,[6] A. Hamed,[47] L-X. Han,[44] R. Haque,[31] J. W. Harris,[57] S. Heppelmann,[36] A. Hirsch,[38] G. W. Hoffmann,[48] D. J. Hofman,[10] S. Horvat,[57] B. Huang,[4] H. Z. Huang,[7] X. Huang,[50] P. Huck,[9] T. J. Humanic,[32] G. Igo,[7] W. W. Jacobs,[18] H. Jang,[24] E. G. Judd,[5] S. Kabana,[45] D. Kalinkin,[19] K. Kang,[50] K. Kauder,[10] H. W. Ke,[4] D. Keane,[22] A. Kechechyan,[21] A. Kesich,[6] Z. H. Khan,[10] D. P. Kikola,[54] I. Kisel,[15] A. Kisiel,[54] D. D. Koetke,[52] T. Kollegger,[15] J. Konzer,[38] I. Koralt,[33] L. K. Kosarzewski,[54] L. Kotchenda,[30] A. F. Kraishan,[46] P. Kravtsov,[30] K. Krueger,[2] I. Kulakov,[15] L. Kumar,[31] R. A. Kycia,[11] M. A. C. Lamont,[4] J. M. Landgraf,[4] K. D. Landry,[7] J. Lauret,[4] A. Lebedev,[4] R. Lednicky,[21] J. H. Lee,[4] C. Li,[42] W. Li,[44] X. Li,[38] X. Li,[46] Y. Li,[50] Z. M. Li,[9] M. A. Lisa,[32] F. Liu,[9] T. Ljubicic,[4] W. J. Llope,[41] M. Lomnitz,[22] R. S. Longacre,[4] X. Luo,[9] G. L. Ma,[44] Y. G. Ma,[44] D. P. Mahapatra,[16] R. Majka,[57] S. Margetis,[22] C. Markert,[48] H. Masui,[26] H. S. Matis,[26] D. McDonald,[49] T. S. McShane,[12] N. G. Minaev,[37] S. Mioduszewski,[47] B. Mohanty,[31] M. M. Mondal,[47] D. A. Morozov,[37] M. K. Mustafa,[26] B. K. Nandi,[17] Md. Nasim,[31] T. K. Nayak,[53] J. M. Nelson,[3] G. Nigmatkulov,[30] L. V. Nogach,[37] S. Y. Noh,[24] J. Novak,[24] S. B. Nurushev,[37] G. Odyniec,[26] A. Ogawa,[4] K. Oh,[39] A. Ohlson,[57] V. Okorokov,[30] E. W. Oldag,[48] D. L. Olvitt, Jr.,[46] B. S. Page,[18] Y. X. Pan,[7] Y. Pandit,[10] Y. Panebratsev,[21] T. Pawlak,[54] B. Pawlik,[34] H. Pei,[9] C. Perkins,[5] P. Pile,[4] M. Planinic,[58] J. Pluta,[54] N. Poljak,[58] K. Poniatowska,[54] J. Porter,[26] A. M. Poskanzer,[26] C. B. Powell,[26] N. K. Pruthi,[35] M. Przybycien,[1] J. Putschke,[56] H. Qiu,[26] A. Quintero,[22] S. Ramachandran,[23] R. Raniwala,[40] S. Raniwala,[40] R. L. Ray,[48] C. K. Riley,[57] H. G. Ritter,[26] J. B. Roberts,[41] O. V. Rogachevskiy,[21] J. L. Romero,[6] J. F. Ross,[12] A. Roy,[53] L. Ruan,[4] J. Rusnak,[14] O. Rusnakova,[13] N. R. Sahoo,[47] P. K. Sahu,[16] I. Sakrejda,[26] S. Salur,[26] J. Sandweiss,[57] E. Sangaline,[6] A. Sarkar,[17] J. Schambach,[48] R. P. Scharenberg,[38] A. M. Schmah,[26] W. B. Schmidke,[4] N. Schmitz,[28] J. Seger,[12] P. Seyboth,[28] N. Shah,[7] E. Shahaliev,[21] P. V. Shanmuganathan,[22] M. Shao,[42] B. Sharma,[35] W. Q. Shen,[44] S. S. Shi,[26] Q. Y. Shou,[44] E. P. Sichtermann,[26] M. Simko,[13] M. J. Skoby,[18] D. Smirnov,[4] N. Smirnov,[57] D. Solanki,[40] P. Sorensen,[4] H. M. Spinka,[2] B. Srivastava,[38] T. D. S. Stanislaus,[52] J. R. Stevens,[27] R. Stock,[15] M. Strikhanov,[30] B. Stringfellow,[38] M. Sumbera,[14] X. Sun,[26] X. M. Sun,[26] Y. Sun,[42] Z. Sun,[25] B. Surrow,[46] D. N. Svirida,[19] T. J. M. Symons,[26] M. A. Szelezniak,[26] J. Takahashi,[8] A. H. Tang,[4] Z. Tang,[42] T. Tarnowsky,[29] J. H. Thomas,[26] A. R. Timmins,[49] D. Tlusty,[14] M. Tokarev,[21] S. Trentalange,[7] R. E. Tribble,[47] P. Tribedy,[53] B. A. Trzeciak,[13] O. D. Tsai,[7] J. Turnau,[34] T. Ullrich,[4] D. G. Underwood,[2] G. Van Buren,[4] G. van Nieuwenhuizen,[27] M. Vandenbroucke,[46] J. A. Vanfossen, Jr.,[22] R. Varma,[17] G. M. S. Vasconcelos,[8] A. N. Vasiliev,[37] R. Vertesi,[14] F. Videbæk,[4] Y. P. Viyogi,[53] S. Vokal,[21] A. Vossen,[18] M. Wada,[48] F. Wang,[38] G. Wang,[7] H. Wang,[4] J. S. Wang,[25] X. L. Wang,[42] Y. Wang,[50] Y. Wang,[10] G. Webb,[4] J. C. Webb,[4] G. D. Westfall,[29] H. Wieman,[26] S. W. Wissink,[18] R. Witt,[51] Y. F. Wu,[9] Z. Xiao,[50] W. Xie,[38] K. Xin,[41] H. Xu,[25] J. Xu,[9] N. Xu,[26] Q. H. Xu,[43] Y. Xu,[42] Z. Xu,[4] W. Yan,[50] C. Yang,[42] Y. Yang,[25] Y. Yang,[9] Z. Ye,[10] P. Yepes,[41] L. Yi,[38] K. Yip,[4] I-K. Yoo,[39] N. Yu,[9] H. Zbroszczyk,[54] W. Zha,[42] J. B. Zhang,[9] J. L. Zhang,[43] S. Zhang,[44] X. P. Zhang,[50] Y. Zhang,[42] Z. P. Zhang,[42] F. Zhao,[7] J. Zhao,[9] C. Zhong,[44] X. Zhu,[50] Y. H. Zhu,[44] Y. Zoulkarneeva,[21] and M. Zyzak[15]

(STAR Collaboration)

[1]*AGH University of Science and Technology, Cracow, Poland*
[2]*Argonne National Laboratory, Argonne, Illinois 60439, USA*
[3]*University of Birmingham, Birmingham, United Kingdom*
[4]*Brookhaven National Laboratory, Upton, New York 11973, USA*
[5]*University of California, Berkeley, California 94720, USA*
[6]*University of California, Davis, California 95616, USA*
[7]*University of California, Los Angeles, California 90095, USA*
[8]*Universidade Estadual de Campinas, Sao Paulo, Brazil*
[9]*Central China Normal University (HZNU), Wuhan 430079, China*
[10]*University of Illinois at Chicago, Chicago, Illinois 60607, USA*
[11]*Cracow University of Technology, Cracow, Poland*
[12]*Creighton University, Omaha, Nebraska 68178, USA*
[13]*Czech Technical University in Prague, FNSPE, Prague 115 19, Czech Republic*

[14]*Nuclear Physics Institute AS CR, 250 68 Řež/Prague, Czech Republic*

[15]*Frankfurt Institute for Advanced Studies FIAS, Germany*

[16]*Institute of Physics, Bhubaneswar 751005, India*

[17]*Indian Institute of Technology, Mumbai, India*

[18]*Indiana University, Bloomington, Indiana 47408, USA*

[19]*Alikhanov Institute for Theoretical and Experimental Physics, Moscow, Russia*

[20]*University of Jammu, Jammu 180001, India*

[21]*Joint Institute for Nuclear Research, Dubna 141 980, Russia*

[22]*Kent State University, Kent, Ohio 44242, USA*

[23]*University of Kentucky, Lexington, Kentucky 40506-0055, USA*

[24]*Korea Institute of Science and Technology Information, Daejeon, Korea*

[25]*Institute of Modern Physics, Lanzhou, China*

[26]*Lawrence Berkeley National Laboratory, Berkeley, California 94720, USA*

[27]*Massachusetts Institute of Technology, Cambridge, Massachusetts 02139-4307, USA*

[28]*Max-Planck-Institut für Physik, Munich, Germany*

[29]*Michigan State University, East Lansing, Michigan 48824, USA*

[30]*Moscow Engineering Physics Institute, Moscow, Russia*

[31]*National Institute of Science Education and Research, Bhubaneswar 751005, India*

[32]*Ohio State University, Columbus, Ohio 43210, USA*

[33]*Old Dominion University, Norfolk, Virginia 23529, USA*

[34]*Institute of Nuclear Physics PAN, Cracow, Poland*

[35]*Panjab University, Chandigarh 160014, India*

[36]*Pennsylvania State University, University Park, Pennsylvania 16802, USA*

[37]*Institute of High Energy Physics, Protvino, Russia*

[38]*Purdue University, West Lafayette, Indiana 47907, USA*

[39]*Pusan National University, Pusan, Republic of Korea*

[40]*University of Rajasthan, Jaipur 302004, India*

[41]*Rice University, Houston, Texas 77251, USA*

[42]*University of Science and Technology of China, Hefei 230026, China*

[43]*Shandong University, Jinan, Shandong 250100, China*

[44]*Shanghai Institute of Applied Physics, Shanghai 201800, China*

[45]*SUBATECH, Nantes, France*

[46]*Temple University, Philadelphia, Pennsylvania 19122, USA*

[47]*Texas A&M University, College Station, Texas 77843, USA*

[48]*University of Texas, Austin, Texas 78712, USA*

[49]*University of Houston, Houston, Texas 77204, USA*

[50]*Tsinghua University, Beijing 100084, China*

[51]*United States Naval Academy, Annapolis, Maryland 21402, USA*

[52]*Valparaiso University, Valparaiso, Indiana 46383, USA*

[53]*Variable Energy Cyclotron Centre, Kolkata 700064, India*

[54]*Warsaw University of Technology, Warsaw, Poland*

[55]*University of Washington, Seattle, Washington 98195, USA*

[56]*Wayne State University, Detroit, Michigan 48201, USA*

[57]*Yale University, New Haven, Connecticut 06520, USA*

[58]*University of Zagreb, Zagreb HR-10002, Croatia*

The J/ψ p_T spectrum and nuclear modification factor (R_{AA}) are reported for $p_T < 5$ GeV/c and $|y| < 1$ from 0% to 60% central Au + Au and Cu + Cu collisions at $\sqrt{s_{NN}} = 200$ GeV at STAR. A significant suppression of p_T-integrated J/ψ production is observed in central Au + Au events. The Cu + Cu data are consistent with no suppression, although the precision is limited by the available statistics. R_{AA} in Au + Au collisions exhibits a strong suppression at low transverse momentum and gradually increases with p_T. The data are compared to high-p_T STAR results and previously published BNL Relativistic Heavy Ion Collider results. Comparing with model calculations, it is found that the invariant yields at low p_T are significantly above hydrodynamic flow predictions but are consistent with models that include color screening and regeneration.

I. INTRODUCTION

Quantum chromodynamics (QCD) predicts a phase transition from hadronic matter to a partonic phase of matter, known as quark-gluon plasma (QGP), at high energy density and temperature. Ultrarelativistic heavy-ion collisions provide a unique tool to create and study this strongly interacting matter that was thought to have populated the universe microseconds after the big bang. The production of heavy quarkonia has been extensively used to probe the medium created in heavy-ion collisions, as these objects are expected to be suppressed in a deconfined medium owing to the Debye color screening of the heavy quark potential [1–4]. Because of their large mass, heavy quarks are primarily created in the initial hard scattering of the collision and thus provide information about the early stages and the evolution of the system. The production of the $c\bar{c}$ bound state-meson $J/\psi(1S)$ has been studied extensively at CERN Super Proton Synchrotron (SPS) [5–7], BNL Relativistic Heavy Ion Collider (RHIC) [8,9], and CERN Large Hadron Collider (LHC) [10,11], and a J/ψ suppression has been observed in heavy-ion collisions.

There are various modifications other than color screening to the production of J/ψ in heavy-ion collisions, such as the recombination of charm quarks [12,13] into bound-state charmonium, and comover absorption [14,15]. The formation time of the J/ψ compared to the time required to emerge from the hot collisions volume may also allow for the escape of high-transverse-momentum (p_T) charmonium from the suppression region [16] (so-called "leakage" effect). However, recent measurements of J/ψ production at high p_T at RHIC [9] show significant suppression in central Au + Au collisions at $\sqrt{s_{NN}} = 200$ GeV for $p_T > 5$ GeV/c. Also, measurements at the LHC [11] show a large suppression at high p_T, which suggests that there is only moderate leakage effect at RHIC and LHC energies. There are additional complications related to the feed-down from B-meson decays and excited states such as ψ' and χ_c. In $p + p$ collisions, excited charmonia states contribute up to 40% of the produced J/ψ yield [17,18], while $B \rightarrow J/\psi$ yield depends strongly on p_T: It is ~2% at $p_T = 1$ GeV/c and increases to 20% for $p_T > 7$ GeV/c [9]. These sources will be modified in a hot medium and further influence the production in heavy-ion collisions. There are also modifications from cold nuclear matter (CNM) effects [19], such as parton scattering [20], modifications to parton distribution functions (PDFs) inside the nucleus (shadowing) [21], and nuclear absorption [22]. To disentangle all of these effects a quantitative understanding of J/ψ production in $p + p$, $p + A$, and $A + A$ is required. The suppression owing to CNM effects has been intensively studied experimentally at Fermilab [23–25], SPS [26–28], and RHIC [29–31] and a few significant effects were established (for instance, an energy dependence of nuclear absorption and a large suppression of ψ' in central $d + $Au collisions at RHIC [30]). However, a comprehensive understanding of the CNM effects is still missing.

An important step towards understanding of J/ψ in-medium interactions is a measurement of J/ψ elliptic flow, which is sensitive to the production mechanism [32]. J/ψ elliptic flow is consistent with zero for $p_T > 2$ GeV/c

[33], indicating that J/ψ is not produced dominantly by coalescence from thermalized (anti-) charm quarks in this p_T range. The collision centrality and transverse momentum dependence of production rates in heavy-ion collisions can provide further insight into the medium effects on J/ψ. Recombination is expected to primarily populate low p_T in central collisions where the charm quark density is the highest, while leakage effect and gluon scattering may enhance high-p_T production. The comparison of production rates in different collision systems, such as Au + Au and Cu + Cu, can provide information about the system-size dependence of the modifications, as J/ψ created in Au + Au collisions will experience higher temperatures and a longer average path length through the surrounding nuclear matter.

In this paper, the results for J/ψ production in Au + Au and Cu + Cu collisions at $\sqrt{s_{NN}} = 200$ GeV at the STAR detector are reported. The J/ψ p_T spectrum and suppression at midrapidity ($|y| < 1$) for $p_T < 5$ GeV/c in 0%–60% centrality collisions are presented, and the transverse momentum and centrality dependence of the results are discussed. These results provide a set of complete spectra from one experiment to cover a wide range of transverse momentum and serve as a consistency check between different experiments in the overlapping kinematics and centralities. This paper describes the experimental setup and data used in this analysis, followed by the analysis methods and associated efficiencies. The results are then discussed and compared to previous data and theoretical calculations.

II. EXPERIMENT AND DATA

The STAR experiment is a large-acceptance multipurpose detector which covers a full azimuth and pseudorapidity range of $|\eta| < 1.8$ [34]. The Au + Au data used in this analysis were obtained using a minimum-bias trigger, which was defined as a coincidence signal in the east and west vertex position detectors (VPDs) [35] located 5.7 m from the interaction point, in the pseudorapidity range of $4.2 \leqslant \eta \leqslant 5.1$. The VPD detector was not available in 2005 when Cu + Cu data were collected, and zero-degree calorimeters (ZDCs) [36] ($|\eta| > 6.3$) were used instead in the minimum-bias trigger. An additional trigger was used in Au + Au collisions to identify central events (0%–5% most central collisions) by requiring a high occupancy in the time-of-flight (TOF) detector [37]. The collision vertex position was determined using a Minuit vertex finder (MinuitVF) [38], and the vertex position along the beamline (V_Z) was required to be within 30 cm of the geometric center of STAR. This range was selected to maximize the uniformity of the detector acceptance. In the off-line analysis, a correlation between the V_Z measured in the VPD detector (V_Z^{VPD}) and the reconstructed collision vertex of $|V_Z - V_Z^{\text{VPD}}| < 3$ cm was required to remove out-of-time (pileup) events in Au + Au collisions. A total of 27×10^6 Cu + Cu and 189×10^6 Au + Au minimum-bias events, recorded in 2005 and 2010, respectively, in 0%–60% centrality collisions and satisfying the requirements described above, were used in this analysis. An additional 85×10^6 events in the 0%–5% most central Au + Au collisions recorded by the central trigger were also analyzed.

TABLE I. The collision centrality definitions, average number of participants and binary collisions, and average impact parameter and their systematic uncertainties from the Glauber model [41] in Au + Au collisions.

Centrality (%)	N_{part}	N_{coll}	b (fm)
0–5	350 ± 3	1071 ± 29	2.3 ± 0.1
5–10	300 ± 7	856 ± 27	4.0 ± 0.2
10–20	236 ± 9	609 ± 31	5.7 ± 0.2
20–30	168 ± 11	377 ± 33	7.3 ± 0.3
30–40	116 ± 11	224 ± 30	8.7 ± 0.3
40–50	76 ± 11	124 ± 25	9.9 ± 0.4
50–60	48 ± 9	64 ± 18	10.9 ± 0.4
0–20	280 ± 6	785 ± 29	4.4 ± 0.2
20–40	142 ± 11	300 ± 31	8.0 ± 0.3
40–60	62 ± 10	95 ± 21	10.4 ± 0.4
0–60	161 ± 9	393 ± 27	7.6 ± 0.3

III. ANALYSIS

J/ψ reconstruction was performed via the dielectron decay channel, $J/\psi \to e^+ + e^-$, with a branching ratio, B, of 5.9% [39]. The primary detector used for tracking and particle identification in this analysis is the time projection chamber (TPC). The barrel electromagnetic calorimeter (BEMC) [40] and the TOF detector [37], were used in the Au + Au data analysis to improve the electron identification.

The TPC is a large-acceptance gas-filled detector and performs the tracking, momentum measurement and particle identification via the ionization energy loss (dE/dx) of charged particles. The TPC has a full azimuthal coverage and a pseudorapidity coverage of $|\eta| < 1.8$.

The charged-particle multiplicity was obtained from the number of reconstructed tracks in the TPC within $|\eta| < 0.5$. Collision centrality was then determined from the measured multiplicity using a Glauber model [41]. For each collision centrality, an average impact parameter, $\langle b \rangle$, average number of participants, $\langle N_{\mathrm{part}} \rangle$, and average number of binary collisions, $\langle N_{\mathrm{coll}} \rangle$ were related to an observed multiplicity range. The centrality definitions in Au + Au collisions are summarized in Table I, and the details on the centrality definitions for Cu + Cu can be found in Ref. [42] and Table II.

We applied basic cuts to ensure good track quality. For Au + Au data, we selected tracks with $|\eta| < 1$, $p_T > 0.2$ GeV/c, at least 16 points in the TPC, and 52% of the maximum number of possible TPC points. The distance of closest approach (DCA) to the collision vertex was required to be less than 2 cm. For Cu + Cu data, we used the same η

TABLE II. The collision centrality definitions, average number of participants and binary collisions and their systematic uncertainties from the Glauber model [41] in Cu + Cu collisions [42].

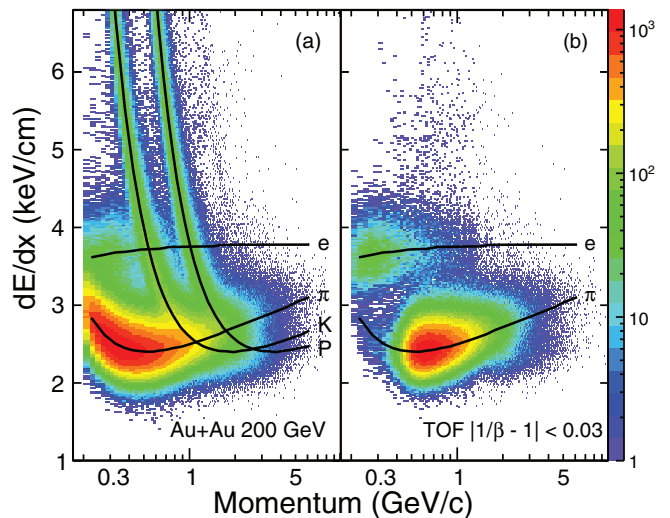| Centrality (%)	N_{part}	N_{coll}
0–20	87 ± 1	156 ± 12
20–40	46 ± 1	63 ± 4
40–60	22 ± 1	23 ± 1
0–60	51 ± 1	80 ± 6

FIG. 1. (Color online) The ionization energy loss dE/dx versus momentum in Au + Au collisions for (a) all charged particles and (b) charged particles with $|1/\beta - 1| < 0.03$. The lines indicate the expected dE/dx for various particles obtained from the Bichsel functions [43].

range but we required at least 25 points in the TPC, 55% of the maximum number of possible TPC points, and DCA < 1 cm. We required electron candidates to have $p_T > 1.1$ GeV/c; it improved signal significance and did not affect the yield much because hadron rejection cuts, described below, removed the majority of electrons with $p_T < 1.1$ GeV

The dE/dx distribution of charged particles in Au + Au collisions is shown versus the momentum in Fig. 1(a). The expected dE/dx was obtained from Bichsel functions [43] and is shown for electrons, pions, kaons, and protons in Fig. 1. The measured dE/dx was normalized to the expected electron dE/dx to obtain $n\sigma_e$, which is approximately Gaussian with $\mu = 0$ and $\sigma = 1$ for electrons,

$$n\sigma_e = \ln \left(\frac{dE/dx|_{\mathrm{measured}}}{dE/dx|_{\mathrm{Bichsel}}} \right) \Big/ \sigma_{dE/dx}, \quad (1)$$

where $dE/dx|_{\mathrm{measured}}$ is the dE/dx measured by the TPC, $dE/dx|_{\mathrm{Bichsel}}$ is the expected dE/dx for electrons obtained from the Bichsel functions, and $\sigma_{dE/dx}$ is the dE/dx resolution. For the Cu + Cu analysis, electrons were required to satisfy $|n\sigma_e| < 2$. The TOF detector was not available when the Cu + Cu data were taken. To remove contamination in the dE/dx-crossover regions in the Cu + Cu analysis, hadrons were rejected using $|n\sigma_p| > 2.5$, $|n\sigma_K| > 2$, and ($n\sigma_\pi > 2.5$) or ($n\sigma_\pi < -3$), for protons, kaons, and pions, respectively. In Au + Au collisions, electrons were identified with the TPC by requiring $-1 < n\sigma_e < 2$, and hadrons were further rejected using the TOF and BEMC, as described below.

The TOF was used in the Au + Au data analysis to improve the electron-hadron discrimination, especially where the electron and hadron dE/dx values overlap. The TOF measures the velocity of charged particles. Electrons were identified by selecting fast particles, which was done by requiring $|1/\beta - 1| < 0.03$, where $\beta = v/c$ [44]. The distribution of
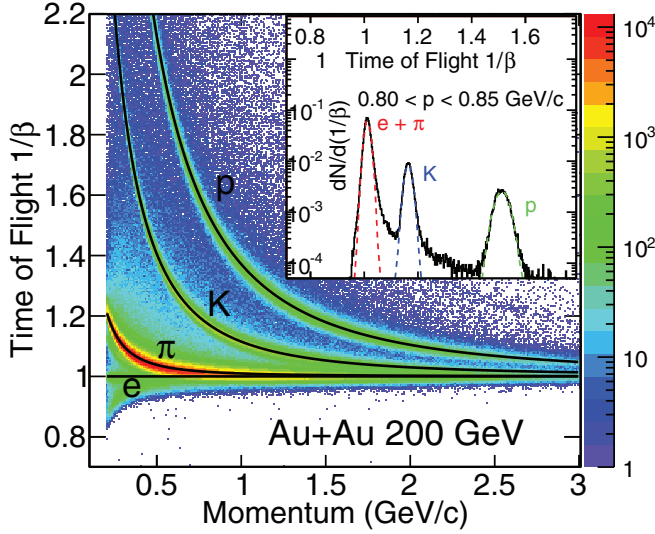
FIG. 2. (Color online) The TOF $1/\beta$ versus momentum for charged particles in Au + Au collisions. The lines indicate the expected $1/\beta$ for various particles. Inset is the $1/\beta$ distribution for $0.8 < p < 0.85$ GeV/c.

FIG. 3. (Color online) The E/p ratio for $3 < p_T < 5$ GeV/c, where E is the single-tower energy from the BEMC, and p is the momentum from the TPC. A high-purity ($>95\%$) electron sample from data (open circles) is compared to a GEANT simulation of the E/p for Monte Carlo electrons (solid triangles). The dashed vertical lines indicate the accepted region ($0.5 < E/p < 1.5$).

$1/\beta$ versus momentum for all charged particles is shown in Fig. 2, and the expected values for electrons, pions, kaons, and protons are also indicated. The inset in the diagram is the $1/\beta$ distribution for $0.8 < p < 0.85$ GeV/c. The electrons and pions are clearly separated from the heavier hadrons such as kaons and protons. Owing to finite time resolution of the TOF, we observe a small number of tracks with $1/\beta < 1$. The TPC has a limited capacity for separation of electrons from kaons and protons below ~ 1 GeV/c. The TOF extends the electron identification capabilities to low p_T by separating electrons and heavier hadrons for $p < 1.5$ GeV/c. The dE/dx distribution for charged particles in Au + Au collisions is shown in Fig. 1(a) before using the TOF and Fig. 1(b) after requiring $|1/\beta - 1| < 0.03$. After using the TOF, the heavier hadrons are removed and the electron band is separated from the remaining hadrons. Pions, which are too light to effectively separate from electrons using the TOF, as seen in Fig. 1(b), are removed using dE/dx by requiring $-1 < n\sigma_e < 2$. At high momentum, the TOF is no longer effective at separating electrons and hadrons. For $p > 1.5$ GeV/c, the BEMC is used to improve the electron identification, as described below.

The BEMC is a lead-scintillator calorimeter segmented into 4800 towers with a tower size of $\Delta\eta \times \Delta\phi = 0.05 \times 0.05$. This detector has a total radiation length of $\sim 20X_0$ and achieves an energy resolution of $dE/E \sim 16\%/\sqrt{E}$ [40]. The BEMC contains a barrel shower maximum detector at a radiation length of $\sim 5X_0$ which consists of two layers of gas wire pad chambers along the η and ϕ planes. It was used to determine the position of energy deposits in the BEMC.

For $p > 1.5$ GeV/c, the BEMC was used to separate electrons from hadrons in Au + Au collisions using the energy-to-momentum ratio, E/p, where p is the momentum obtained from the TPC and E the single-tower energy obtained from the BEMC. The energy-to-momentum ratio is shown in Fig. 3 for a high-purity ($>95\%$) electron sample from data,
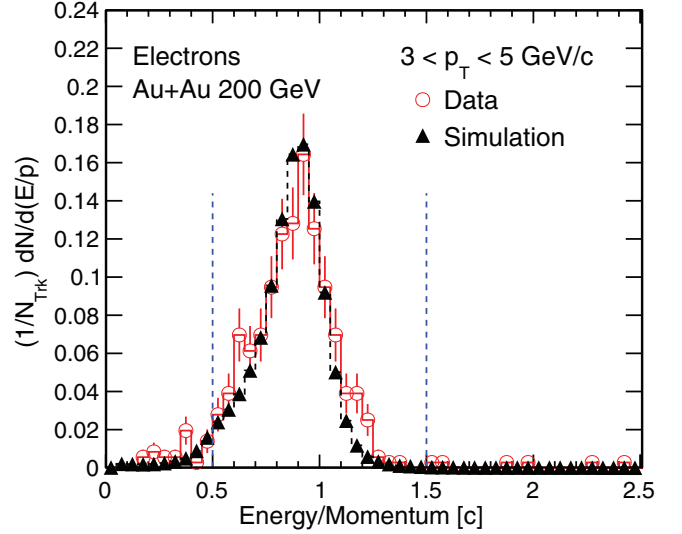
which was obtained by using dE/dx, TOF, and selecting photonic electrons (from photon conversion in the detector material or from Dalitz decays of π and η mesons).

Comparison of the measured electron E/p to that for Monte Carlo electrons from a full GEANT simulation [45] shows good agreement. There is a non-Gaussian tail at low E/p seen in real and simulated data owing to energy loss in neighboring towers when an electron strikes near the tower edge. The BEMC was used to discriminate electrons and hadrons by requiring $0.5 < E/p < 1.5$.

IV. SIGNAL AND CORRECTIONS

The opposite-sign dielectron invariant mass spectrum is shown for Au + Au collisions with $p_T < 5$ GeV/c and $|y| < 1$ in Fig. 4, and was obtained from (a) minimum-bias data in 0%–60% centrality and (b) central-triggered data in 0%–5% centrality. Figure 5 shows similar distributions for Cu + Cu collisions for minimum-bias (0%–60%) and central (0%–20%) collisions. The combinatorial background was estimated using same-sign pairs from the same event and opposite-sign pairs from mixed events. The opposite-sign mixed-event background was normalized to the same-sign, same-event background in a mass range of $2.6 < m_{ee} < 3.6$ GeV/c^2 and subtracted from the dielectron invariant mass spectrum to obtain the J/ψ signal. An effect of possible different acceptance for same-sign and opposite-sign pairs was studied for the same data set in Ref. [46]. The ratio of same-sign and opposite-sign pairs is unity for $m_{ee} > 0.5$ GeV/c^2; thus the impact on the mixed-event background normalization is negligible.

A signal-to-background ratio of $1:20$ was achieved in 0%–60% centrality Cu + Cu collisions. This has substantially improved with the removal of γ-converting material of the inner-detector subsystems and the addition of the TOF. A
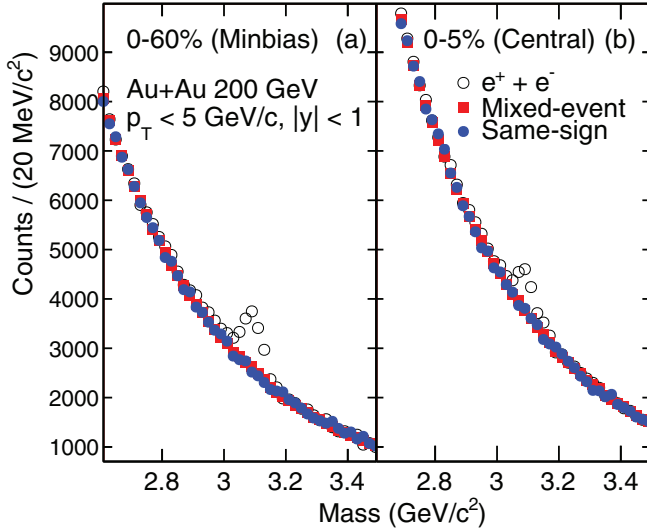
FIG. 4. (Color online) The opposite-sign dielectron invariant mass distribution (open circles) from (a) minimum-bias trigger data in 0%–60% and (b) central trigger data in 0%–5% centrality Au + Au collisions at $\sqrt{s_{NN}} = 200$ GeV. The mixed-event background (squares) was normalized to the like-sign background (open circles) and subtracted from the opposite-sign distribution to obtain the J/ψ signal.

FIG. 6. (Color online) The J/ψ signal for $|y| < 1$ after mixed-event background subtraction (open circles) from (a) minimum-bias trigger data in 0%–60% centrality and (b) central trigger data in 0%–5% centrality Au + Au collisions at $\sqrt{s_{NN}} = 200$ GeV. The J/ψ signal shape obtained from a simulation (dashed line) is combined with a linear background (dot-dashed line) and is fitted to the data (solid line).

signal-to-background ratio of $1 : 5$ in 0%–60% centrality Au + Au collisions was achieved, increasing from $1 : 11$ in 0%–5% to $1 : 1$ in 40%–60% centrality collisions.

The dielectron invariant mass spectrum after background subtraction in Au + Au and Cu + Cu collisions is shown in Figs. 6 and 7. The data are compared to the J/ψ signal shape obtained from a simulation, combined with a straight

line (in the case of Au + Au) or second-order polynomial (for Cu + Cu) background. The J/ψ signal shape was determined using a GEANT simulation of the detector response to Monte Carlo J/ψ particles embedded into real data events and is due to the resolution of the TPC and bremsstrahlung of the daughter electrons in the detector.
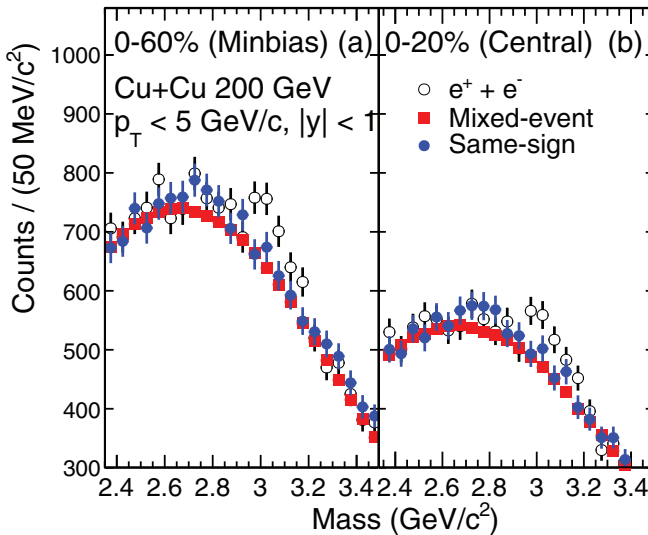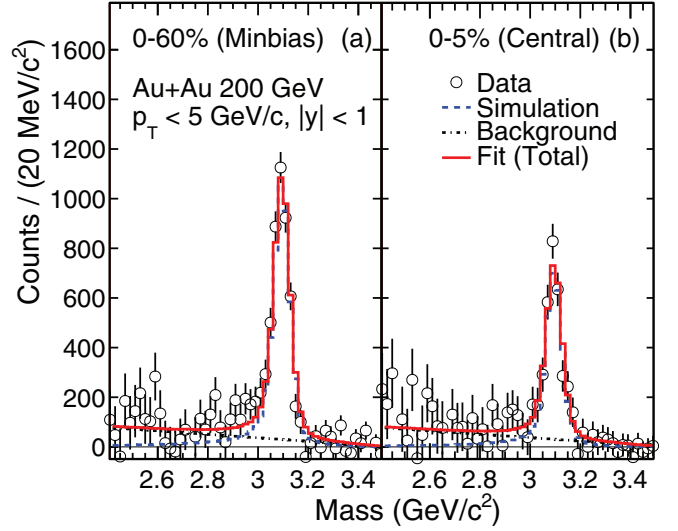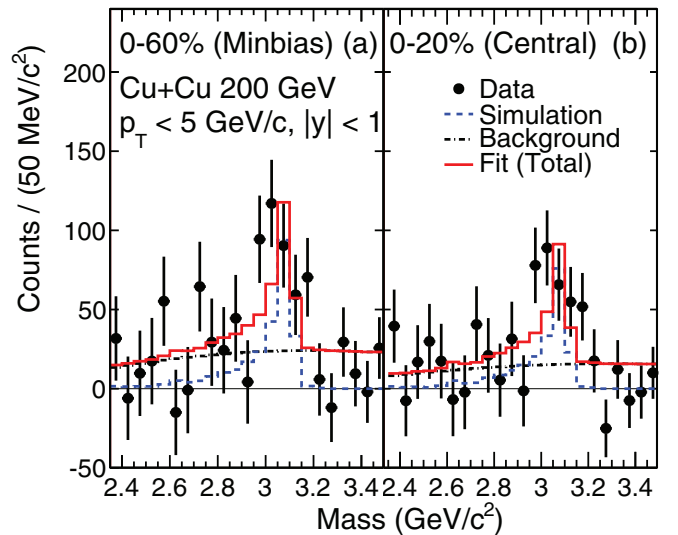

FIG. 5. (Color online) The opposite-sign dielectron invariant mass distribution (open circles) from (a) minimum-bias (0%–60% centrality) and (b) central (0%–20% centrality) Cu + Cu collisions at $\sqrt{s_{NN}} = 200$ GeV. The mixed-event background (squares) was normalized to the like-sign background (open circles) and subtracted from the opposite-sign distribution to obtain the J/ψ signal.

FIG. 7. (Color online) The J/ψ signal for $|y| < 1$ after mixed-event background subtraction (open circles) from minimum-bias (0%–60% centrality) and (b) central (0%–20% centrality) Cu + Cu collisions at $\sqrt{s_{NN}} = 200$ GeV. The J/ψ signal shape obtained from a simulation (dashed line) is combined with a second-order polynomial background (dot-dashed line) and is fitted to the data (solid line).
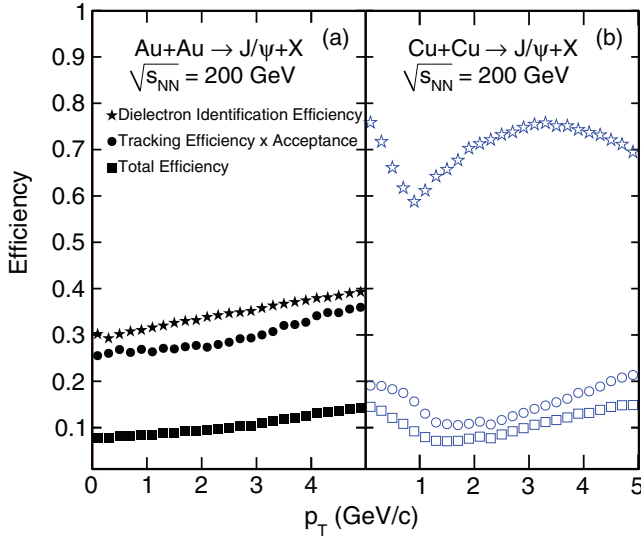
FIG. 8. (Color online) The J/ψ total efficiency (squares), tracking efficiency and acceptance (circles), and dielectron identification efficiency (stars) for 0%–60% centrality (a) Au + Au (solid symbols) and (b) Cu + Cu (open symbols) collisions. The shape of the dielectron identification efficiency in (b) is attributable to a proton rejection cut (see text for details).

The yield was calculated by counting the entries in a mass window of $2.7 < m_{ee} < 3.2 \, \mathrm{GeV}/c^2$ as a function of collision centrality and transverse momentum. To account for residual background in Au + Au collisions, a straight line was included in the J/ψ signal shape fit to the J/ψ signal in the data. In Cu + Cu collisions, the simulated J/ψ signal shape does not reproduce the data well and we used a Gaussian instead. Furthermore, residual background had a different shape owing to the p_T cut for electrons (especially for low-p_T J/ψ); thus, a second-order polynomial was used to estimate this background. The residual background was then subtracted from the counts in the given mass range.

The fraction of J/ψ counts outside of the mass range of $2.7 < m_{ee} < 3.2 \, \mathrm{GeV}/c^2$ was determined from the J/ψ signal shape obtained from simulation and was found to be 7%–8% for both Au + Au and Cu + Cu collisions. This was used to correct the number of J/ψ counts. A total of 370 ± 90 J/ψ were reconstructed in Cu + Cu collisions with signal significance $S/\Delta S = 4$, where ΔS is the uncertainty on the measured signal S. In Au + Au, 5636 ± 295 J/ψ were reconstructed in minimum-bias 0%–60% collisions with a significance of 19, while 4050 ± 322 J/ψ were reconstructed in central-trigger 0%–5% centrality collisions with a significance of 13.

The detector acceptance and tracking efficiency were determined using a Monte Carlo GEANT simulation and are shown in Fig. 8 for 0%–60% centrality collisions in (a) Au + Au and (b) Cu + Cu. The tracking efficiency is higher in Au + Au compared to Cu + Cu data due to stringent p_T and track quality cuts for electron candidates. The electron identification efficiency in Cu + Cu exhibits a strong p_T dependence owing to the hadron rejection requirements placed on dE/dx, which cause a drop in the identification efficiency for $p_T \sim 1$ GeV/c. The identification efficiency is lower

TABLE III. The systematic uncertainties for 0%–60% centrality in Au + Au and Cu + Cu collisions.

Source	Relative uncertainty (%)	
	Cu + Cu	Au + Au
eID (TPC)	3	6
eID (TOF)	–	3
eID (BEMC)	–	14
Efficiency	4	7
Yield	13	10
Total	14	21
N_{coll}	7	7
σ_{inel}	8	8
σ_{pp} (stat.)	3	3
σ_{pp} (syst.)	7	7

in Au + Au due to the TOF matching efficiency of $\sim 65\%$ and BEMC matching efficiency of $\sim 85\%$. The TOF and BEMC matching efficiencies were calculated from the ratio of all electron candidates to those which were successfully matched to the TOF and BEMC, respectively. The total J/ψ efficiency and acceptance correction is obtained by combining the tracking efficiency and acceptance with the total identification efficiency of both electron daughters and is $\sim 8\%$–15% (5%–15%) in Au + Au (Cu + Cu) collisions.

The systematic uncertainties in the Au + Au analysis include uncertainties from the particle identification efficiency using the TPC (6%), TOF (3%), and BEMC (15%), the tracking efficiency and acceptance correction (7%), and the yield extraction methods (10%). The uncertainty on the yield extraction was determined by varying the width of the J/ψ signal shape from simulation, by varying the mass range in which the fit was performed, and by comparing the yields obtained from fitting and from counting. An additional 4% uncertainty was included to account for the contribution from radiative decay $J/\psi \to e^+ + e^- + \gamma$ [47], which are not included in the simulation.

In the case of the Cu + Cu analysis, the main sources of systematic uncertainty were from the estimation of the combinatorial background ($\sim 13\%$–26%), and the tracking efficiency and acceptance correction (4%). The particle identification was performed using the TPC only, and resulted in an uncertainty of $\sim 3\%$. The systematic uncertainties in the Au + Au and Cu + Cu data for 0%–60% centrality and integrated p_T are summarized in Table III. The centrality and transverse momentum dependence of the total systematic uncertainties, quoted as one standard deviation, are reflected in the results shown in Sec. V.

V. RESULTS

The J/ψ invariant yield is defined as

$$\frac{B}{2\pi p_T}\frac{d^2N}{dy\,dp_T} = \frac{1}{2\pi p_T \Delta p_T \Delta y}\frac{N_{J/\psi}}{N_{\mathrm{Ev}}\varepsilon}, \quad (2)$$

where $N_{J/\psi}$ is the uncorrected number of reconstructed J/ψ, B is branching ratio, N_{Ev} is the number of events, and ε is
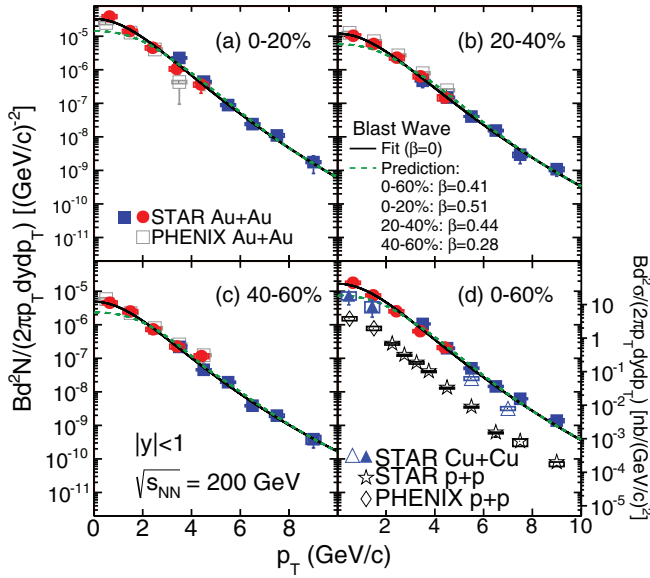
FIG. 9. (Color online) The invariant yield versus transverse momentum for $|y| < 1$ in (a) 0%–20%, (b) 20%–40%, (c) 40%–60%, and (d) 0%–60% centrality in Au + Au collisions (solid circles). The results are compared to high-p_T ($3 < p_T < 10$ GeV/c) results from STAR [9] (solid squares) and PHENIX data [8] (open squares). Also shown is the yield in 0%–60% centrality Cu + Cu collisions for low p_T (solid triangles) and high p_T [48] (open triangles). The models are described in the text [49,50]. The J/ψ cross section in $p + p$ collisions is also shown in (d) at STAR (stars) and PHENIX [51] (diamonds), and the scale is indicated on the right axis.

the total efficiency and acceptance correction factor. The p_T dependence of the J/ψ invariant yield from this analysis is shown in Fig. 9(d) for $p_T < 5$ GeV/c and $|y| < 1$ in 0%–60% centrality Au + Au and Cu + Cu collisions and compared to the high-p_T J/ψ yield for Cu + Cu collisions [48] (for $5 < p_T < 8$ GeV/c) and Au + Au collisions from STAR [9] ($3 < p_T < 10$ GeV/c). The bars represent the statistical uncertainty, and the boxes represent the systematic uncertainty. The results for 0%–20%, 20%–40%, and 40%–60% centrality Au + Au collisions are also shown in Figs. 9(a)–9(c) and are compared to high-p_T data. The STAR data in Au + Au collisions are consistent with the previously published results from PHENIX [8] for $p_T < 5$ GeV/c and $|y| < 0.35$.

The J/ψ invariant yield in Au + Au collisions shown in Fig. 9 was compared to a Tsallis blast wave (TBW) model assuming that the J/ψ flows like lighter hadrons (dashed line) [49,50], i.e., assuming the radial flow velocity $\beta = 0.41$ for 0%–60% central collisions, 0.51 for 0%–20%, 0.44 for 20%–40%, and 0.28 for 40%–60% events. The normalization for the TBW model was determined from the high-p_T data. The TBW model qualitatively agrees with our data for $p_T > 2$ GeV/c: χ^2 over number of degrees of freedom (NDF), χ^2/NDF $= 7.2/4$ for 0%–60% central events, taking into account statistical and systematic uncertainties. However, it underestimates the yield at lower p_T: χ^2/NDF $= 100/9 = 11.1$ for $0 < p_T < 10$ GeV/c in 0%–60% central collisions. The STAR data were also fitted with a TBW model in $0 < p_T < 10$ GeV/c that assumes a zero radial flow velocity
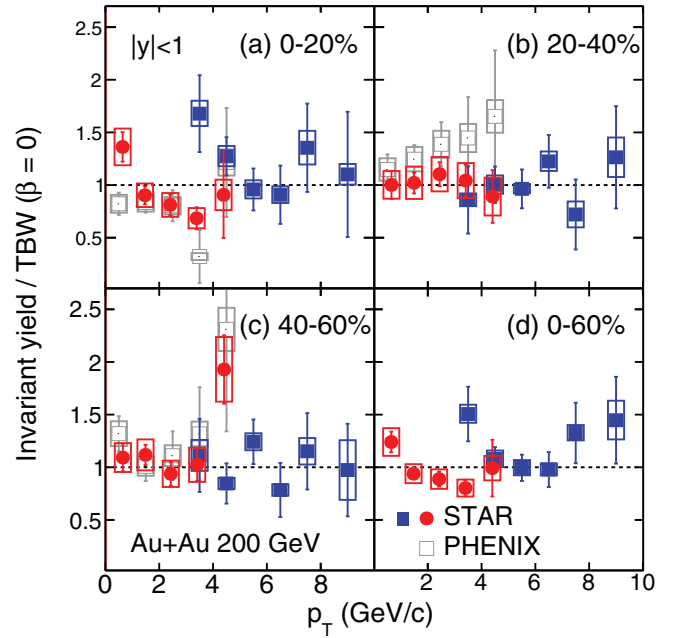

FIG. 10. (Color online) Ratio of invariant yield from Fig. 9 to predictions of Tsallis blast wave model with radial flow $\beta = 0$ [50]. Data are shown as a function of transverse momentum for $|y| < 1$ in (a) 0%–20%, (b) 20%–40%, (c) 40%–60%, and (d) 0%–60% centrality in Au + Au collisions.

(solid line) [49]. Figure 10 shows a ratio of J/ψ invariant yield in Au + Au collisions to the TBW model with $\beta = 0$. The agreement with the data at low p_T is better for semicentral
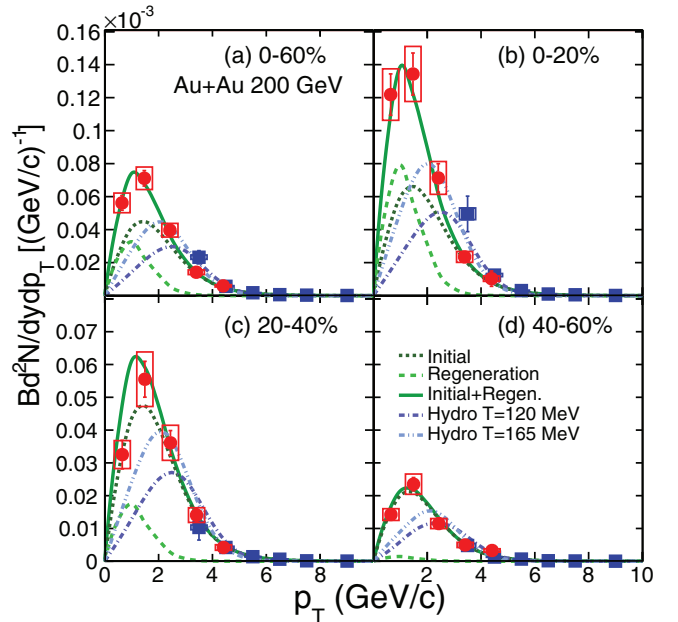

FIG. 11. (Color online) The J/ψ yield versus transverse momentum for $|y| < 1$ in (a) 0%–60%, (b) 0%–20%, (c) 20%–40%, and (d) 40%–60% collision centrality in Au + Au collisions (solid circles). The data are compared to high-p_T ($3 < p_T < 10$ GeV/c) results from STAR [9] (solid squares). The models are described in the text [52,53].

TABLE IV. The J/ψ invariant yield $\frac{B}{2\pi p_T}\frac{d^2N}{dydp_T}$ and nuclear modification factor as a function of transverse momentum for $|y| < 1$ in Au + Au collisions at $\sqrt{s_{NN}} = 200$ GeV with (A) statistical, (B) systematic, and (C) global uncertainties. The yield and corresponding uncertainties are in units of $(\text{GeV}/c)^{-2}$.

Centrality	p_T (GeV/c)	$\langle p_T\rangle$ (GeV/c)	$\frac{B}{2\pi p_T}\frac{d^2N}{dydp_T}$	(A)	+(B)	−(B)	R_{AA}	(A)	+(B)	−(B)	(C)
0–60	0–1	0.64	17.89×10^{-6}	1.42×10^{-6}	$+1.89\times10^{-6}$	-1.90×10^{-6}	0.50	0.04	+0.05	−0.05	0.09
0–60	1–2	1.47	7.54×10^{-6}	0.50×10^{-6}	$+0.72\times10^{-6}$	-0.73×10^{-6}	0.41	0.03	+0.04	−0.04	0.08
0–60	2–3	2.42	2.52×10^{-6}	0.20×10^{-6}	$+0.26\times10^{-6}$	-0.26×10^{-6}	0.56	0.04	+0.06	−0.06	0.11
0–60	3–4	3.40	0.64×10^{-6}	0.06×10^{-6}	$+0.06\times10^{-6}$	-0.06×10^{-6}	0.49	0.05	+0.05	−0.05	0.08
0–60	4–5	4.40	0.21×10^{-6}	0.06×10^{-6}	$+0.02\times10^{-6}$	-0.02×10^{-6}	0.67	0.18	+0.08	−0.08	0.12
0–20	0–1	0.64	38.78×10^{-6}	3.99×10^{-6}	$+4.96\times10^{-6}$	-4.97×10^{-6}	0.55	0.06	+0.07	−0.07	0.09
0–20	1–2	1.47	14.25×10^{-6}	1.35×10^{-6}	$+1.77\times10^{-6}$	-1.77×10^{-6}	0.39	0.04	+0.05	−0.05	0.07
0–20	2–3	2.41	4.54×10^{-6}	0.55×10^{-6}	$+0.63\times10^{-6}$	-0.63×10^{-6}	0.50	0.06	+0.07	−0.07	0.09
0–20	3–4	3.39	1.07×10^{-6}	0.16×10^{-6}	$+0.15\times10^{-6}$	-0.15×10^{-6}	0.40	0.06	+0.06	−0.06	0.06
0–20	4–5	4.39	0.36×10^{-6}	0.16×10^{-6}	$+0.06\times10^{-6}$	-0.06×10^{-6}	0.58	0.26	+0.09	−0.09	0.10
20–40	0–1	0.65	10.35×10^{-6}	1.38×10^{-6}	$+1.35\times10^{-6}$	-1.36×10^{-6}	0.38	0.05	+0.05	−0.05	0.08
20–40	1–2	1.49	5.89×10^{-6}	0.58×10^{-6}	$+0.88\times10^{-6}$	-0.88×10^{-6}	0.42	0.04	+0.06	−0.06	0.08
20–40	2–3	2.44	2.30×10^{-6}	0.24×10^{-6}	$+0.34\times10^{-6}$	-0.34×10^{-6}	0.67	0.07	+0.10	−0.10	0.14
20–40	3–4	3.41	0.64×10^{-6}	0.09×10^{-6}	$+0.10\times10^{-6}$	-0.10×10^{-6}	0.63	0.09	+0.10	−0.10	0.11
20–40	4–5	4.41	0.15×10^{-6}	0.04×10^{-6}	$+0.03\times10^{-6}$	-0.03×10^{-6}	0.62	0.17	+0.13	−0.13	0.12
40–60	0–1	0.65	4.53×10^{-6}	0.54×10^{-6}	$+0.57\times10^{-6}$	-0.57×10^{-6}	0.53	0.06	+0.07	−0.07	0.15
40–60	1–2	1.49	2.49×10^{-6}	0.22×10^{-6}	$+0.33\times10^{-6}$	-0.33×10^{-6}	0.57	0.05	+0.07	−0.07	0.16
40–60	2–3	2.43	0.73×10^{-6}	0.09×10^{-6}	$+0.10\times10^{-6}$	-0.10×10^{-6}	0.67	0.08	+0.09	−0.09	0.19
40–60	3–4	3.41	0.23×10^{-6}	0.03×10^{-6}	$+0.04\times10^{-6}$	-0.04×10^{-6}	0.71	0.11	+0.11	−0.11	0.19
40–60	4–5	4.41	0.12×10^{-6}	0.02×10^{-6}	$+0.02\times10^{-6}$	-0.02×10^{-6}	1.55	0.26	+0.24	−0.25	0.43

and peripheral events (χ^2/NDF = 2.9/9 for 20%–40% and χ^2/NDF = 13.1/9 for 40%–60% centrality classes). There is still some discrepancy for central and minimum-bias events: χ^2/NDF = 26.5/9 for 0%–20% central events and χ^2/NDF = 21.7/9 for 0%–60% events. It suggests that the J/ψ has a small radial flow or that there may be contributions from recombination. Recombination is expected to happen at low transverse momenta; thus, it would increase the J/ψ yield at low p_T.

The J/ψ yield, $Bd^2N/dydp_T$, is shown in Fig. 11 for various collision centralities. The results are compared to predictions from viscous hydrodynamics using a J/ψ decoupling temperature of $T = 120$ MeV and $T = 165$ MeV (dot-dashed lines) [53]. The predictions assume a zero chemical potential for J/ψ at kinetic freeze-out, and the scale of the predictions is determined from a fit to the data in the p_T range of $p_T < 5$ GeV/c. The data favor the higher decoupling temperature; however, the hydrodynamic calculations fail to describe the

low p_T J/ψ yield ($p_T < 2$ GeV/c) and predict a large J/ψ elliptic flow at high-p_T, while the measured elliptic flow for $p_T > 2$ GeV/c is consistent with zero [33].

The data are also compared to theoretical predictions that include J/ψ suppression due to color screening and the statistical regeneration of charm quarks in Au + Au by Liu *et al.* [52] (dashed line). The contribution from initial production dominates in peripheral events. Regeneration becomes more significant in central events and at low p_T. The predictions describe the p_T spectrum across the entire measured transverse momentum range ($p_T < 10$ GeV/c).

The J/ψ yield is summarized in Tables IV–VII for Au + Au and Cu + Cu collisions, respectively. The uncertainties are separated into (A) statistical and (B) systematic uncertainties.

To quantify J/ψ suppression in $A + A$ collisions, we calculate a nuclear modification factor R_{AA}. R_{AA} is obtained from the ratio of the J/ψ yield in $A + A$ and $p + p$ collisions,

TABLE V. The J/ψ invariant yield and nuclear modification factor as a function of centrality for $|y| < 1$ in Au + Au collisions at $\sqrt{s_{NN}} = 200$ GeV with (A) statistical, (B) systematic, and (C) global uncertainties.

Centrality	p_T (GeV/c)	BdN/dy	(A)	+(B)	−(B)	R_{AA}	(A)	+(B)	−(B)	(C)
0–5	0–5	464.38×10^{-6}	32.43×10^{-6}	$+56.67\times10^{-6}$	-56.82×10^{-6}	0.43	0.03	+0.05	−0.05	0.06
5–10	0–5	447.06×10^{-6}	56.24×10^{-6}	$+52.95\times10^{-6}$	-53.10×10^{-6}	0.52	0.07	+0.06	−0.06	0.07
10–20	0–5	266.75×10^{-6}	25.70×10^{-6}	$+29.06\times10^{-6}$	-29.13×10^{-6}	0.44	0.04	+0.05	−0.05	0.06
20–30	0–5	174.38×10^{-6}	14.01×10^{-6}	$+19.50\times10^{-6}$	-19.55×10^{-6}	0.46	0.04	+0.05	−0.05	0.07
30–40	0–5	110.44×10^{-6}	8.77×10^{-6}	$+10.26\times10^{-6}$	-10.28×10^{-6}	0.49	0.04	+0.05	−0.05	0.09
40–50	0–5	69.85×10^{-6}	5.19×10^{-6}	$+6.74\times10^{-6}$	-6.76×10^{-6}	0.56	0.04	+0.05	−0.05	0.13
50–60	0–5	45.15×10^{-6}	3.52×10^{-6}	$+4.30\times10^{-6}$	-4.32×10^{-6}	0.70	0.05	+0.07	−0.07	0.21

TABLE VI. The J/ψ invariant yield $\frac{B}{2\pi p_T}\frac{d^2N}{dy dp_T}$ and nuclear modification factor as a function of transverse momentum for $|y| < 1$ in Cu + Cu collisions at $\sqrt{s_{NN}} = 200$ GeV with (A) statistical, (B) systematic, and (C) global uncertainties. The yield and corresponding uncertainties are in units of $(\mathrm{GeV}/c)^{-2}$.

Centrality	p_T(GeV/c)	$\langle p_T \rangle$(GeV/c)	$\frac{B}{2\pi p_T}\frac{d^2N}{dy dp_T}$	(A)	+(B)	−(B)	R_{AA}	(A)	+(B)	−(B)	(C)
0–60	0–1	0.47	7.48×10^{-6}	3.57×10^{-6}	2.0×10^{-6}	2.0×10^{-6}	1.03	0.49	0.27	0.27	0.19
	1–2	1.43	3.56×10^{-6}	1.88×10^{-6}	1.27×10^{-6}	1.27×10^{-6}	0.95	0.50	0.34	0.34	0.17

where the latter is scaled by the average number of binary collisions $\langle N_{\mathrm{coll}} \rangle$ in A + A,

$$R_{AA} = \frac{\sigma_{\mathrm{inel}}}{\langle N_{\mathrm{coll}} \rangle} \frac{d^2 N_{AA}/dy dp_T}{d^2 \sigma_{pp}/dy dp_T}, \qquad (3)$$

where σ_{inel} is the inelastic cross section in $p + p$ collisions, $\sigma_{\mathrm{inel}} = 42 \pm 3$ mb, N_{AA} is J/ψ yield in A + A collisions, and $d^2\sigma_{pp}/dy dp_T$ is the J/ψ cross section in $p + p$ collisions.

The integrated J/ψ cross section in $p + p$ collisions, used as a baseline, was obtained by combining the STAR data for $p_T > 2$ GeV/c [9] and low-p_T ($p_T < 2$ GeV/c) mid-rapidity measurements from PHENIX [51]. The global uncertainty combines the statistical and systematic uncertainty on the J/ψ $p + p$ cross section (σ_{pp}) [9,51], the uncertainty on the inelastic cross section in $p + p$ collisions (σ_{inel}) at STAR (8%) [55] and PHENIX (10%) [51], and the uncertainty in N_{coll} shown in Table I. The PHENIX results (for $|y| < 0.35$) were extrapolated to the STAR acceptance ($|y| < 1$) assuming that $d\sigma/dy$ is constant at $|y| < 1$. We estimated the systematic error due to the extrapolation by fitting J/ψ $d\sigma/dy$ distribution [56] with Gaussian and $A \exp[-b \cosh(cy)]$ functions (where A, b, and c are free parameters), and then calculating the cross section at $y = 0$ using STAR rapidity coverage. We found that this systematic error is about 1%. Figure 9(d) shows the combined cross section in $p + p$ collisions with the magnitude indicated by the scale on the right vertical axis. We present here only the PHENIX $p + p$ data points used in the R_{AA} calculations for the sake of clarity; nonetheless, STAR and PHENIX results agree very well in the overlapping p_T range [9].

The transverse momentum dependence of the nuclear modification factor is shown in Fig. 12 for various collision centralities in Au + Au and in Fig. 13 for 0%–60% centrality Cu + Cu collisions. The bars and boxes on the data points represent the statistical and systematic uncertainties, respectively. The statistical and systematic uncertainties on the J/ψ cross section in $p + p$ collisions are indicated by the hatched and solid bands, respectively. The boxes on the vertical axes represent the uncertainty on N_{coll}, combined with the uncertainty on the inelastic cross section in $p + p$ collisions at STAR of 8% [55]. The Au + Au and Cu + Cu

data are compared to the STAR high-p_T results [9] for $|y| < 1$, and to PHENIX results [8,54] in $|y| < 0.35$. The data in Fig. 12 are compared to theoretical predictions based on the suppression of J/ψ owing to color screening and the statistical regeneration of charm quarks in Au + Au and Cu + Cu by Zhao and Rapp (solid line [32,57]) and Liu *et al.* (dashed line) [52]). The model of Zhao and Rapp also includes B feed-down and formation-time effect (the leakage effect) to J/ψ production. Owing to limited statistics, STAR results at low p_T are inconclusive regarding possible suppression of J/ψ in Cu + Cu collisions. The Au + Au data exhibit an increase in R_{AA} for $p_T > 1$ GeV/c for all centralities. Both models are able to reproduce the data. A significant suppression is observed for $p_T < 3$ GeV/c in Au + Au collisions ($R_{AA} < 0.6$) for all centralities.

The centrality dependence of the J/ψ nuclear modification factor, R_{AA}, is shown in Fig. 14 as a function of N_{part}. The STAR data for $p_T < 5$ GeV/c in Au + Au and Cu + Cu collisions are shown for $|y| < 1$. The uncertainty on N_{coll} in Au + Au and Cu + Cu is indicated by the hatched point-to-point bands. The global uncertainty combines the uncertainty on the J/ψ cross section in $p + p$ collisions and the uncertainty on the inelastic cross section in $p + p$ collisions at STAR and is indicated by the band on the right vertical axis.

PHENIX previously reported a significant suppression in midcentral and central Cu + Cu collisions [54]. The STAR Cu + Cu data exhibit no suppression within sizable uncertainties. However, the difference between STAR and PHENIX results is less than 1.5 standard deviation when systematic and statistical uncertainties are taken into account.

The Au + Au data are suppressed for all centralities. The suppression increases with collision centrality up to $N_{\mathrm{part}} \sim 150$ and then saturates. The data are compared to the PHENIX results in Au + Au collisions with $|y| < 0.35$ [8]. These results are consistent for peripheral and semicentral collisions ($N_{\mathrm{part}} < 250$). For the most central collisions (0%–5% and 0%–10%) the STAR data show a smaller suppression compared to PHENIX results. Nevertheless, the difference between these measurements is not statistically significant, taking into account statistical and systematic uncertainties: We test the consistency between these results using the z

TABLE VII. The J/ψ invariant yield and nuclear modification factor for $|y| < 1$ in Cu + Cu collisions at $\sqrt{s_{NN}} = 200$ GeV with (A) statistical, (B) systematic, and (C) global uncertainties.

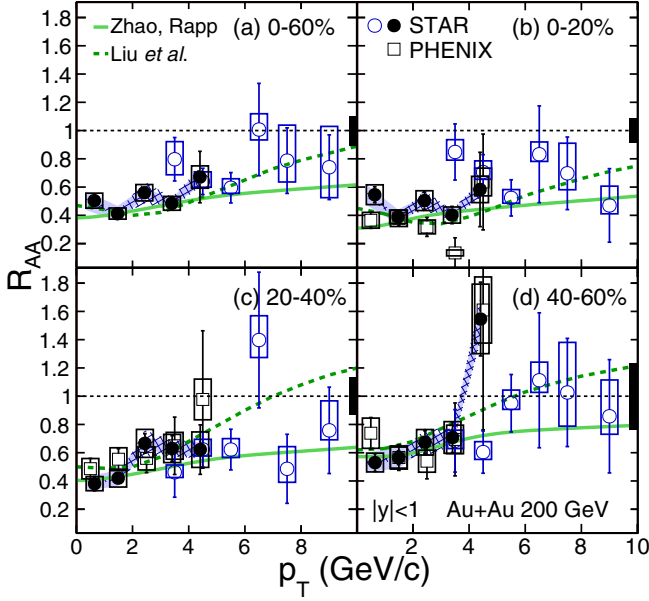| Centrality	p_T(GeV/c)	BdN/dy	(A)	+(B)	−(B)	R_{AA}	(A)	+(B)	−(B)	(C)
0–20	0–5	192×10^{-6}	61×10^{-6}	59×10^{-6}	59×10^{-6}	1.23	0.39	0.37	0.37	0.15
0–60	0–5	79×10^{-6}	22×10^{-6}	11×10^{-6}	11×10^{-6}	0.98	0.35	0.17	0.17	0.15

FIG. 12. (Color online) The J/ψ nuclear modification factor versus transverse momentum for $|y| < 1$ and $p_T < 5$ GeV/c for (a) 0%–60%, (b) 0%–20%, (c) 20%–40%, and (d) 40%–60% centrality Au + Au collisions (solid circles). The data are compared with STAR high-p_T ($5 < p_T < 10$ GeV/c) results [9] and PHENIX results [8] in $|y| < 0.35$ (open squares). The statistical and systematic uncertainties on the baseline J/ψ cross section in $p + p$ collisions are indicated by the hatched and solid bands, respectively. Boxes on the vertical axes represent the uncertainty on N_{coll} combined with the uncertainty on the inelastic cross section in $p + p$ collisions.
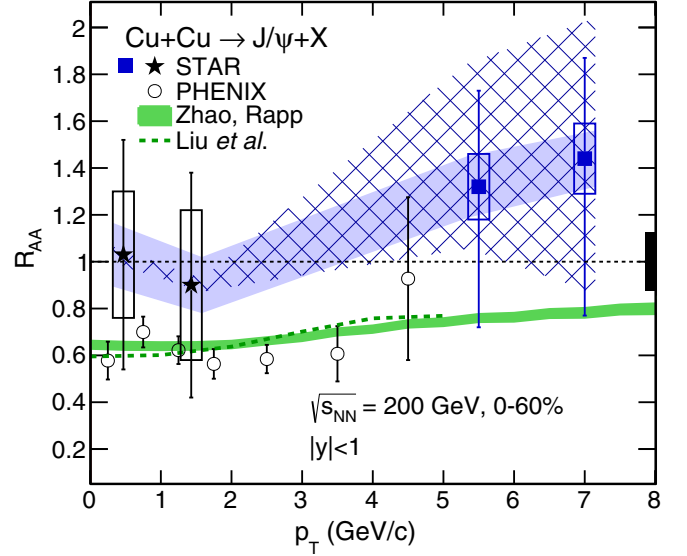

FIG. 13. (Color online) The J/ψ nuclear modification factor versus p_T for $|y| < 1$ and $p_T < 5$ GeV/c in Cu + Cu collisions (solid stars). The data are compared to high-p_T results from STAR (open stars) [9] and PHENIX data with $|y| < 0.35$ [54] (open circles). The bars and boxes on the data points represent the statistical and systematic uncertainties, respectively. The statistical and systematic uncertainties on the J/ψ cross section in $p + p$ collisions are indicated by the hatched and solid bands, respectively. The box on the vertical axis represents the uncertainty on N_{coll} combined with the uncertainty on the inelastic cross section in $p + p$ collisions.
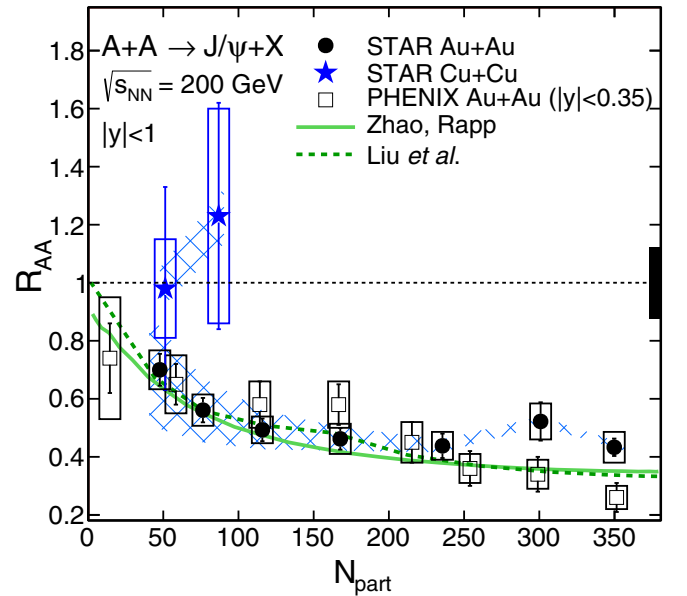
test: $z = (\mu_1 - \mu_2)/\sqrt{\sigma_1^2 + \sigma_2^2}$, where μ and σ is a mean and standard deviation of a given sample, $\sigma = \sqrt{\sigma_{\text{stat.}}^2 + \sigma_{\text{syst.}}^2}$, and the two samples are assumed to be independent of one another and have a normal distribution. The difference between STAR and PHENIX results for 0%–5% most central events is 2σ and 1.5σ for 5%–10% central events.

The centrality dependence of R_{AA} for $p_T < 5$ GeV/c from theoretical predictions for J/ψ production including the suppression of J/ψ owing to color screening and the statistical regeneration of charm quarks in Au + Au collisions from Zhao and Rapp [32] and Liu *et al.* [52] are also shown. The predictions are able to describe the data well across the collision centrality range, and we are unable to distinguish between the models. The J/ψ nuclear modification factor is summarized in Tables IV and V for Au + Au collisions and Tables VI and VII for Cu + Cu collisions. The uncertainties are separated into (A) statistical, (B) systematic, and (C) global uncertainties.

VI. SUMMARY

We presented J/ψ production at low p_T ($p_T < 5$ GeV/c) in Au + Au and Cu + Cu collisions at $\sqrt{s_{NN}} = 200$ GeV. These results, combined with STAR high-p_T data, provides coverage of J/ψ production in Au + Au collisions for a wide p_T range of $0 < p_T < 10$ GeV/c. Comparisons of p_T spectra

FIG. 14. (Color online) The nuclear modification factor versus N_{part} for J/ψ with $|y| < 1$ and $p_T < 5$ GeV/c in Au + Au collisions (solid circles) and Cu + Cu collisions (solid stars). The data are compared to PHENIX data with $|y| < 0.35$ (open squares) and theoretical predictions (solid line [32] and dashed line [52]). The uncertainty in $p + p$ collisions is described by the box along the vertical axis, and the hatched bands indicate the uncertainty from N_{coll}.

with TBW model suggest that the J/ψ has a small radial flow or significant contribution from recombination at low p_T.

In the case of Au + Au, we observed a strong suppression at low and moderate p_T ($p_T < 3$ GeV/c) with $R_{AA} < 0.6$ for all centralities. The suppression decreases with increasing p_T for $p_T > 2$ GeV/c. Measurement of the nuclear modification factor as a function of centrality indicates a strong suppression in central and semicentral collisions. Centrality and p_T dependence of R_{AA} are well described by the models assuming an interplay between color screening and regeneration in the hot medium, as well as possible J/ψ escape effects. A detailed investigation of low-p_T production, including a high-statistics analysis of elliptic flow, may provide a better understanding of this process.

[1] T. Matsui and H. Satz, Phys Lett. B **178**, 416 (1986).
[2] S. Digal, P. Petreczky, and H. Satz, Phys. Rev. D **64**, 094015 (2001).
[3] F. Karsch, D. Kharzeev, and H. Satz, Phys. Lett. B **637**, 75 (2006).
[4] P. Braun-Munzinger and J. Stachel, Nature (London) **448**, 302 (2007).
[5] M. C. Abreu *et al.* (NA38 Collaboration), Phys. Lett. B **449**, 128 (1999).
[6] M. C. Abreu *et al.* (NA50 Collaboration), Phys. Lett. B **410**, 327 (1997).
[7] R. Arnaldi *et al.* (NA60 Collaboration), Phys. Rev. Lett. **99**, 132302 (2007).
[8] A. Adare *et al.* (PHENIX Collaboration), Phys. Rev. Lett. **98**, 232301 (2007).
[9] L. Adamczyk *et al.* (STAR Collaboration), Phys. Lett. B **722**, 55 (2013).
[10] B. Abelev *et al.* (ALICE Collaboration), Phys. Rev. Lett. **109**, 072301 (2012).
[11] S. Chatrchyan *et al.* (CMS Collaboration), J. High Energy Phys. 05 (2012) 063.
[12] P. Braun-Munzinger and J. Stachel, Phys. Lett. B **490**, 196 (2000).
[13] L. Grandchamp and R. Rapp, Nucl. Phys. A **709**, 415 (2002).
[14] S. Gavin and R. Vogt, Nucl. Phys. A **610**, 442 (1996).
[15] A. Capella *et al.*, Phys. Lett. B **393**, 431 (1997).
[16] F. Karsch and P. Petronzio, Z. Phys. C **37**, 627 (1988).
[17] A. Adare *et al.* (PHENIX Collaboration), Phys. Rev. D **85**, 092004 (2012).
[18] A. Zoccoli *et al.* (HERA-B Collaboration), Eur. Phys. J. C **43**, 179 (2005).
[19] R. Vogt, Phys. Rev. C **71**, 054902 (2005).
[20] S. Gavin and M. Gyulassy, Phys. Lett. B **214**, 241 (1988).
[21] J. V. Noble, Phys. Rev. Lett. **46**, 412 (1981).
[22] V. Tram and F. Arleo, Eur. Phys. J. C **61**, 847 (2009).
[23] D. Alde, H. Baer, T. Carey, G. Garvey, A. Klein *et al.*, Phys. Rev. Lett. **66**, 133 (1991).
[24] M. Leitch *et al.* (E772 and E789 Collaboration), Nucl. Phys. A **544**, 197 (1992).
[25] M. Leitch *et al.* (NuSea Collaboration), Phys. Rev. Lett. **84**, 3256 (2000).
[26] B. Alessandro *et al.* (NA50 Collaboration), Eur. Phys. J. C **33**, 31 (2004).
[27] B. Alessandro *et al.* (NA50 Collaboration), Eur. Phys. J. C **39**, 335 (2005).
[28] R. Arnaldi *et al.* (NA60 Collaboration), Phys. Lett. B **706**, 263 (2012).
[29] A. Adare *et al.* (PHENIX Collaboration), Phys. Rev. C **87**, 034904 (2013).
[30] A. Adare *et al.* (PHENIX Collaboration), Phys. Rev. Lett. **111**, 202301 (2013).
[31] A. Adare *et al.* (PHENIX Collaboration), Phys. Rev. Lett. **107**, 142301 (2011).
[32] X. Zhao and R. Rapp, Phys. Rev. C **82**, 064905 (2010).
[33] L. Adamczyk *et al.* (STAR Collaboration), Phys. Rev. Lett. **111**, 052301 (2013).
[34] K. H. Ackermann *et al.*, Nucl. Instrum. Methods Phys. Res., Sect. A **499**, 624 (2003).
[35] W. J. Llope *et al.*, Nucl. Instrum. Methods Phys. Res., Sect. A **522**, 252 (2004).
[36] C. Adler *et al.*, Nucl. Instrum. Methods Phys. Res., Sect. A **499**, 433 (2003).
[37] W. Llope, Nucl. Instrum. Methods Phys. Res., Sect. A **661** (Suppl. 1), S110 (2012).
[38] R. Reed *et al.*, J. Phys.: Conf. Ser. **219**, 03020 (2010).
[39] J. Beringer *et al.* (Particle Data Group), Phys. Rev. D **86**, 010001 (2012).
[40] M. Beddo *et al.*, Nucl. Instrum. Methods Phys. Res., Sect. A **499**, 725 (2003).
[41] M. L. Miller, K. Reygers, S. J. Sanders, and P. Steinberg, Annu. Rev. Nucl. Part. Sci. **57**, 205 (2007).
[42] B. I. Abelev *et al.* (STAR Collaboration), Phys. Lett. B **673**, 183 (2009).
[43] H. Bichsel, Nucl. Instrum. Methods Phys. Res., Sect. A **562**, 154 (2006).
[44] M. Shao *et al.*, Nucl. Instrum. Methods Phys. Res., Sect. A **558**, 419 (2006).
[45] B. I. Abelev *et al.* (STAR Collaboration), Phys. Rev. C **79**, 034909 (2009).
[46] L. Adamczyk *et al.* (STAR Collaboration), arXiv:1402.1791.
[47] A. Spiridonov, arXiv:hep-ex/0510076.
[48] B. I. Abelev *et al.* (STAR Collaboration), Phys. Rev. C **80**, 041902 (2009).

[49] Z. Tang, Y. Xu, L. Ruan, G. van Buren, F. Wang, and Z. Xu, Phys. Rev. C **79**, 051901 (2009).

[50] Z. Tang, L. Yi, L. Ruan, M. Shao, H. Chen *et al.*, Chin. Phys. Lett. **30**, 031201 (2013).

[51] A. Adare *et al.* (PHENIX Collaboration), Phys. Rev. D **82**, 012001 (2010).

[52] Y. Liu, Z. Qu, N. Xu, and P. Zhuang, Phys. Lett. B **678**, 72 (2009).

[53] U. W. Heinz and C. Shen (private communication).

[54] A. Adare *et al.* (PHENIX Collaboration), Phys. Rev. Lett. **101**, 122301 (2008).

[55] J. Adams *et al.* (STAR Collaboration), Phys. Rev. Lett **91**, 172302 (2003).

[56] A. Adare *et al.* (PHENIX Collaboration), Phys. Rev. Lett. **98**, 232002 (2007).

[57] X. Zhao and R. Rapp, Phys. Lett. B **664**, 253 (2008).